WILEY-VCH

DOI: 10.1002/ ((please add manuscript number))
Article type: Full Paper

Impact of monovalent cation halide additives on the structural and optoelectronic properties of $CH_3NH_3PbI_3$ perovskite

Mojtaba Abdi-Jalebi, M. Ibrahim Dar, Aditya Sadhanala, Satyaprasad P. Senanayak, Marius Franckevičius, Neha Arora, Yuanyuan Hu, Mohammad Khaja Nazeeruddin, Shaik M. Zakeeruddin, Michael Grätzel,* Richard H. Friend**

M Abdi-Jalebi, Dr. Aditya Sadhanala, Dr. S. P. Senanayak, Dr. Y. Hu, Prof. R. H. Friend
Cavendish Laboratory, Department of Physics, University of Cambridge, JJ Thomson Avenue, Cambridge CB3 0HE, UK

E-mail: rhf10@cam.ac.uk; ibrahim.dar@epfl.ch; michael.graetzel@epfl.ch

Dr. M. I. Dar, Dr. N. Arora, Dr. S. M. Zakeeruddin, Prof. M. Grätzel
Laboratory of Photonics and Interfaces, Institute of Chemical Sciences and Engineering, École Polytechnique Fédérale de Lausanne, CH-1015 Lausanne, Switzerland

Dr. M. Franckevičius,
Center for Physical Sciences and Technology, Savanorių Ave. 231, LT-02300 Vilnius, Lithuania

Prof. M. K. Nazeeruddin
Group for Molecular Engineering of Functional Materials, Institute of Chemical Sciences and Engineering, École Polytechnique Fédérale de Lausanne, CH-1015-Lausanne, Switzerland

Abstract

We report the influence of monovalent cation halide additives on the optical, excitonic and electrical properties of $CH_3NH_3PbI_3$ perovskite. Monovalent cation halide with similar ionic radii to Pb^{2+}, including Cu^+, Na^+ and Ag^+, were added to explore possibility of doping. We observed significant reduction of sub-bandgap optical absorption and lower energetic disorder along with a shift in the Fermi level of the perovskite in the presence of these cations. The bulk hole mobility of the additive based perovskites as estimated using the space charge limited current method exhibited an increase of up to an order of magnitude compared to the pristine perovskites with a significant decrease in the activation energy. Consequentially, enhancement in the photovoltaic parameters of additive-based solar cells was achieved. We observed an increase in open circuit voltage for AgI (~1.02 vs 0.95 V for the pristine) and photocurrent density for NaI and CuBr based solar cells (≈23 vs 21 $mA.cm^{-2}$ for the pristine). This enhanced photovoltaic performance could be attributed to the formation of uniform and continuous perovskite film, better conversion and loading of perovskite as well as the enhancement in the bulk charge transport along with a minimization of disorder, pointing towards possible surface passivation.

Keywords: Monovalent cation halide, additives, $CH_3NH_3PbI_3$ Perovskite, doping, surface passivation

1. Introduction

Nowadays, organic–inorganic metal halide perovskites have been receiving tremendous attention owing to their facile synthesis[1], low temperature deposition[2], capability to make flexible devices[3], and extraordinary optical and electronic properties[4,5]. Organic-inorganic metal halide perovskites have a cubic framework structure with general formula ABX_3 (where A is an organic cation, B a divalent metal ion and X a halide ion Cl, Br or I or any mixture thereof). Perovskite-sensitized solar cell employing a liquid electrolyte was first documented by Miyasaka and co-workers, and reported an efficiency of 3.8% for $CH_3NH_3PbI_3$ based solar cell[1]. In recent years, perovskite solar cells (PSC) have shown a paradigm shift in photovoltaic technology, mainly by adopting device configuration ranging from mesoscopic semiconducting TiO_2[6,7] or insulating Al_2O_3 scaffolds[8], to the planar heterojunction (PHJ) architecture[3,9]. Recently, a certified power conversion efficiency of over 20%[10] has been reported through optimizing device design, material interfaces, processing techniques and chemical composition of perovskite materials[11–13]. These recent developments further demonstrate the promising potential of PSC to compete with silicon solar cells in the photovoltaic markets[14].

In general, there are four methods, which includes one step spin deposition[15], vacuum vapor deposition[9], two-step deposition technique[6,16], and patterning thin film[17] to prepare the hybrid organic-inorganic perovskite film. So far, solution processed PSC show the highest efficiency and stability[12,18]. However, achieving good quality solution processed $CH_3NH_3PbI_3$ films on top of mesoporous TiO_2 (ms-TiO_2) with high uniformity and smoothness is a challenge. In many PSC, a non-continuous perovskite film is usually obtained, where pinholes can introduce shunting pathways limiting the device performance. Recent studies show that by upon addition of excess organic component (methyl ammonium iodide) much larger crystalline domains can be created[8], and smoother films can be formed than those processed from a stoichiometric mixture of CH_3NH_3I and PbI_2[19]. In addition, it is found that changing the anions from halide to acetate in

the lead source of perovskite solution has an effective influence on the perovskite crystal growth and therefore improves the film quality[20]. On the other hand, hybrid $CH_3NH_3PbI_3$ doped with Sn^{2+}, Sr^{2+}, Cd^{2+} and Ca^{2+} in the position of the Pb^{2+} ion, are also known to affect both the crystalline phase and the band gap energy[21]. A complete understanding of these issues is hence critically important for advancing our understanding of perovskite semiconductors and solar cell performance.

Despite the rapid rise in the PSC performance, the fundamental properties of organic–inorganic trihalide perovskites pertaining to the formation of perovskite are not yet well understood. Various investigations have focused on tuning the band gap of absorber material by changing the ratio of cations[22], anions[5] or the divalent metal[23,24]. But, the effect of precursor composition on the perovskite crystal growth, film formation, coverage and thus on the device performance, is yet to be investigated in detail[20,25,26].

In this work, we explore the effect of adding small amount of monovalent cation halide based salts including NaI, CuBr, CuI and AgI into the perovskite precursor solution on morphology, charge transport, excitonic and optical properties of $CH_3NH_3PbI_3$ perovskite. To the best of our knowledge, the incorporation of $CH_3NH_3PbI_3$ with aforementioned salts has not been reported so far. Morphological characterization based on field emission scanning electron microscopy (FE-SEM) determined that shape and coverage of the $CH_3NH_3PbI_3$ structures prepared in the presence of additives is considerably different from an additive-free reference. In addition, samples were characterized using X-ray diffraction (XRD) to study crystalline phases present in the samples and the extent of lead halide conversion into perovskite in presence of additives. Comprehensive studies on optical properties of additive based perovskite were carried out using photothermal deflection spectroscopy (PDS), UV-visible absorption and photoluminescence (PL). In addition, kelvin probe force microscopy (KPFM) and space charge limited current (SCLC) technique were used to characterise influence of aforementioned additives on electrical properties of $CH_3NH_3PbI_3$

perovskite. Finally, fabrication of solar cells based on the incorporated monovalent cation in perovskite structure reveals an improvement in power conversion efficiency (PCE) reaching 15.6% which can be ascribed to the improvement in the conversion reaction, optical, excitonic and electrical properties of $CH_3NH_3PbI_3$.

2. Results and discussion

In this study, $CH_3NH_3PbI_3$ perovskite samples were synthesized using sequential two-steps deposition process[6] in which 0.02 mol.L^{-1} of different additives including NaI, CuBr, CuI and AgI were added into the 1.2 mol.L^{-1} PbI_2 solution in N, N-dimethylformamide (DMF). In this procedure, the $CH_3NH_3PbI_3$ is formed onto ~250 nm thick TiO_2 photoanode films by spin coating DMF solution of PbI_2 followed by dip coating in a solution of isopropyl alcohol containing methylamonium iodide (MAI) under optimized conditions.

2.1. Morphological characterization

To understand the impact of these additives on the surface morphology of the PbI_2 and $CH_3NH_3PbI_3$ deposited on mesoporous TiO_2 photoanode, field emission scanning electron microscopy (FESEM) was employed. The top view SEM image confirms that the mesoporous TiO_2 is covered by an overlayer of PbI_2 (Figure 1, left-side). It is noteworthy that a significant change in the morphology of PbI_2 overlayer is observed while adding NaI to its solution (Figure 1d) and a rough and highly porous overlayer of PbI_2 containing branched large crystals was formed. This morphological difference was also evident from the macroscopic image (Figure S1a) as the respective PbI_2 film including NaI is relatively more scattering compared to pristine lead iodide film (Figure S1b).

In addition, the presence of CuBr does not make any significant difference in the morphology of PbI_2 (Figure 1b) whereas, in case of CuI and AgI based samples, we, obtain a uniform and pinhole free overlayer (Figure 1c, e). The right side of Figure 1 displays top-view SEM images of $CH_3NH_3PbI_3$ films obtained after the conversion of pristine and additive based PbI_2 films.

Comparative SEM analysis brought out variations in perovskite morphology. Pristine samples revealed the formation of large tetragonal-shaped perovskite crystals on top of the ms-TiO_2 film while relatively better surface coverage of mesoporous-TiO_2 with perovskite crystal is observed for CuBr based sample (Figure 1b). Moreover, considerable improvement in the surface coverage of titania scaffold with uniform and continuous perovskite structure is observed in the presence of CuI and AgI additives (Figure 1c, e). Particularly, in the case of $CH_3NH_3PbI_3$ incorporated with AgI, the perovskite crystals are better-connected. In Figure 2d, large crystals of NaI based perovskite sample with asymmetric shape are observed which infers that the nature of PbI_2 film can define the morphological properties of resulting perovskite films.

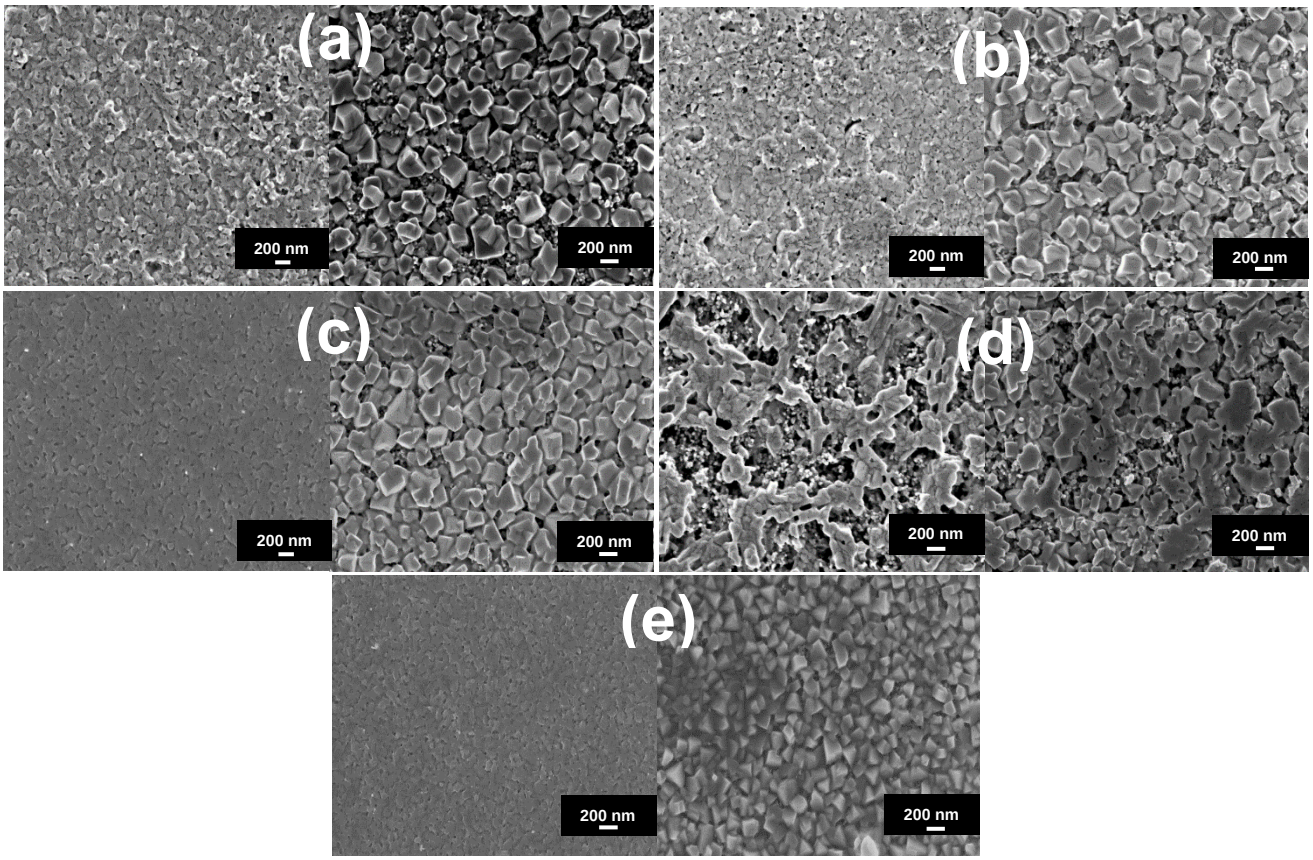

Figure 1. Top-view SEM images of PbI_2 (left side) and $CH_3NH_3PbI_3$ (right side) structures: (a) pristine, (b) CuBr-, (c) CuI-, (d) NaI- and (e) AgI-based perovskite samples deposited on a mesoporous TiO_2-coated FTO.

We further characterized the perovskite films obtained from pristine and additives based lead halide precursors by atomic force microscopy (AFM) (Figure 2). The root mean-squared roughness of the pristine, CuBr, CuI, NaI, and AgI based perovskite films was found to be 51.2, 28.2, 21.3, 63.0 and 17.7nm, respectively. Expectedly, perovskite film including NaI additive exhibits a branched morphology with the highest roughness whereas the roughness of CuI and

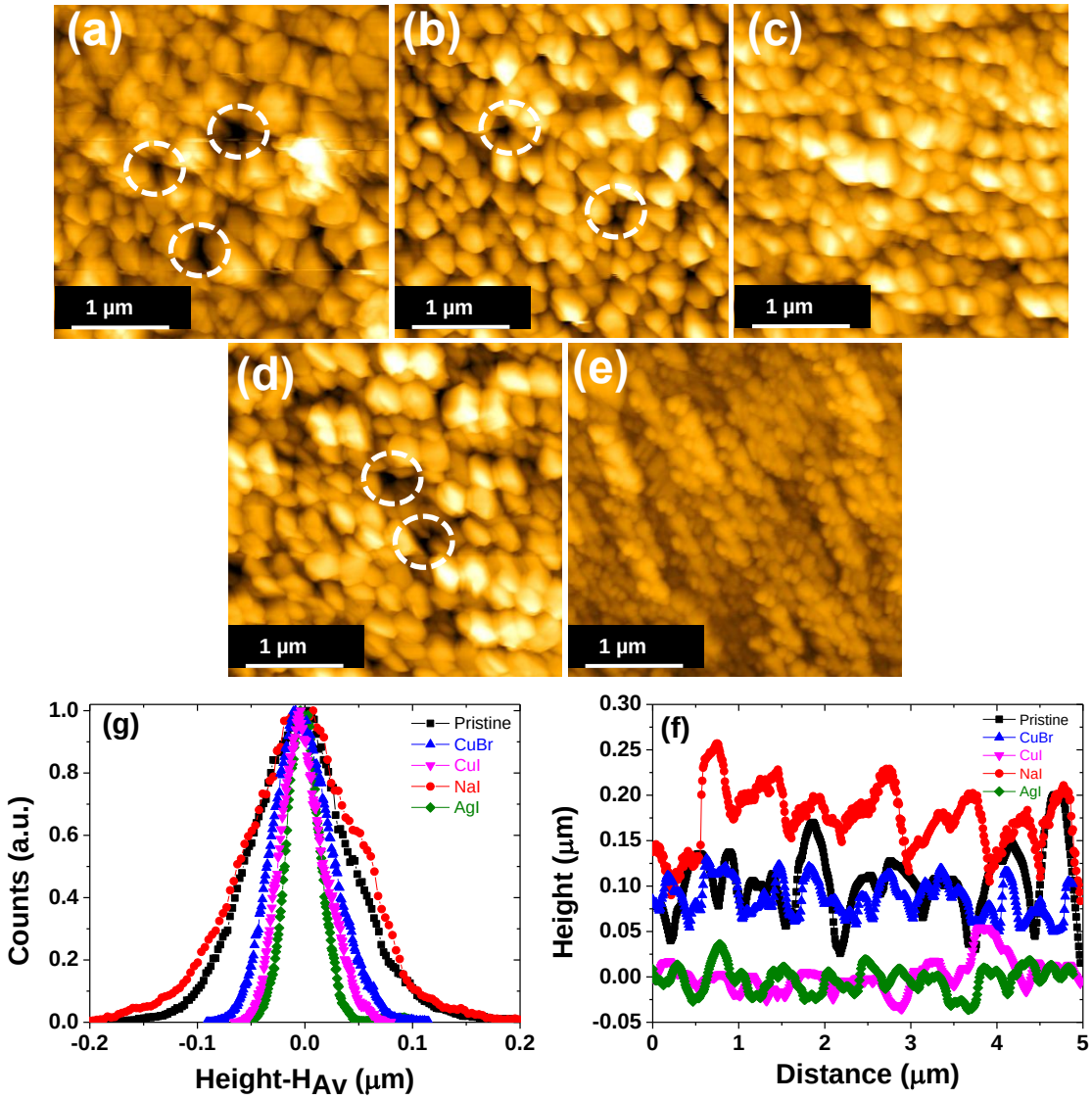

Figure 2. AFM images of perovskite structures: (a) pristine, (b) CuBr-, (c) CuI-, (d) NaI- and (e) AgI-based $CH_3NH_3PbI_3$ deposited on a mesoporous TiO_2-coated FTO. Examples of pinholes in pristine, CuBr and NaI derived films are circled, which are notably absent in the CuI and AgI based films. Line segments from each scan (f) and the height distribution (g) around the average height, H_{Av}, show the exceptional smoothness of the AgI and CuI-derived films.

AgI based films are greatly reduced compared with the pristine sample, as is evident from both, AFM line segments (Figure 2f) and height distribution analysis (Figure 2g). It is worth emphasizing that the perovskite films including CuI and AgI additives are nearly pinhole free as compared to pristine and other samples (see circles in Figure 2a, b and d). It is encouraging that by adding small amount of additives inside the lead halide precursor solution, the smoothness of the perovskite films prepared by two-step deposition method enhanced strongly.

2.2. Structural characterization

To investigate the effect of monovalent cation halide additives on the crystal structure of PbI_2 and $CH_3NH_3PbI_3$ perovskite, X-ray diffraction spectroscopy was carried out. In Figure 3, we show the X-ray diffraction patterns of pristine- and additive based-PbI_2 and -$CH_3NH_3PbI_3$ films, respectively. These diffraction patterns are indexed based on the standard JCPD file number 01-072-1147 and 21-1272 for FTO and TiO_2, respectively, as well as using literature data for PbI_2 and $CH_3NH_3PbI_3$ perovskite[27].

According to the literature data, it is evident that the PbI_2 deposited by spin-coating from DMF solution crystallizes in the form of the hexagonal 2H polytype[28]. The presence of the most intense diffraction peak (2θ=12.60) indexable to the (001) lattice planes (Figure 3a, black curve), is indicative of preferential growth of PbI_2 crystallites along the c-axis.

It should be noted that CuBr, CuI and AgI-based perovskite films show similar intensity in various diffraction peaks to the pristine one, however the NaI-based sample depicts sharper diffraction peaks for the (001) lattice plane. Moreover, sharpness of the diffraction peak (001) for NaI based sample compare to broad one for the pristine can be attributed to the larger crystallite size of PbI_2 structures which demonstrates that NaI additive influences the growth of PbI_2 structures (Figure 1d).

The conversion of PbI_2 into CH_3NH_3I was ascertained by X-ray diffraction (XRD). All the

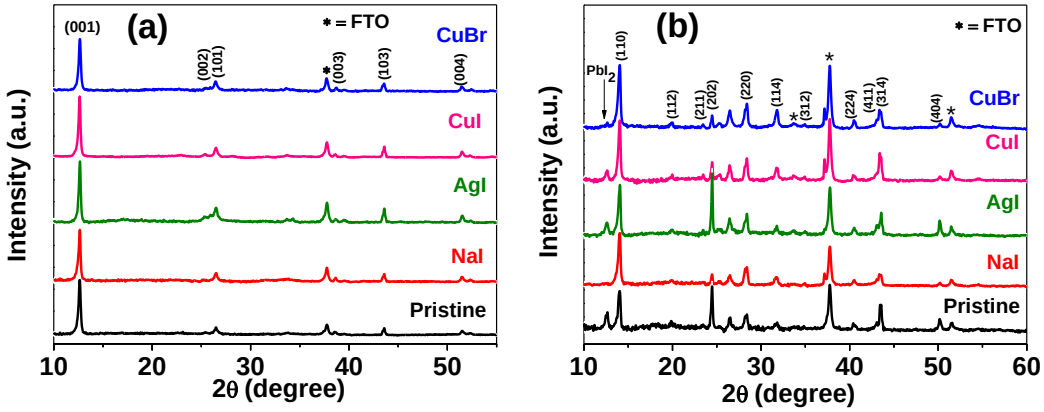

Figure 3. X-ray diffraction spectra of pristine and additives based (a) PbI_2 and (b) $CH_3NH_3PbI_3$ perovskite that is grown on mesoporous TiO_2 film which is deposited on the FTO coated glass.

diffraction peaks present in the XRD patterns could be indexed to the tetragonal phase of the $CH_3NH_3PbI_3$ perovskite[29]. In addition, presence of diffraction peak (2θ=12.6) attributable to PbI_2 indicates the presence of unconverted PbI_2 within the $CH_3NH_3PbI_3$ film. XRD patterns obtained from the additives based samples perfectly match with that of pristine $CH_3NH_3PbI_3$ sample which confirms that the presence of additives do not alter the crystal structure of the final $CH_3NH_3PbI_3$ material (Figure 3b). However, based on an analysis using the Scherrer equation,[30] the average crystallite sizes of pristine, CuBr, CuI, NaI and AgI based perovskite vary and were estimated to be 62±10, 73±12, 56±9, 95±14 and 45±11 nm, respectively. It is important to note that these values are based on the assumption of spherical perovskite crystals.

In addition, it was also observed that the diffraction peak of PbI_2 in NaI-based sample vanished and its intensity dropped significantly in CuBr-based one. This observation can be attributed to the following two reasons; first, presence of additive is enhancing the extent of conversion reaction of PbI_2 into $CH_3NH_3PbI_3$ which eventually leaves less amount of unreacted PbI_2. Secondly, morphological modifications of PbI_2 overlayer, i.e., from a relatively compact layer to a more porous one, facilitates the conversion further. As the NaI-based sample reveals a full conversion of PbI_2 into the $CH_3NH_3PbI_3$, which has been already established from the XRD

pattern, the second hypothesis seems more feasible. It is to be noted that significant variations in the morphology of PbI_2 overlayer were observed in SEM analysis (Figure 1). On the other hand, a relatively high intense PbI_2 diffraction peak is observed in the XRD patterns of CuI and AgI based samples. This further confirms that the morphology of PbI_2 overlayer strongly influences the extent of PbI_2 conversion into $CH_3NH_3PbI_3$.

2.3. Optical spectroscopy

2.3.1. UV-visible Absorption

Steady state optical absorption and PL spectra of pristine and additives based methylammonium lead iodide perovskite films, are presented in Figure 4a. The optical absorption spectrum of pristine $CH_3NH_3PbI_3$ perovskite film (solid black line) shows broad absorption band covering the entire visible spectral range with a band edge at around 780 nm. Large extinction coefficient and typical spectral behaviour of methylammonium lead iodide perovskite film is consistent with the previous reports[31]. The comparative analysis of absorption spectra of pristine and additives based $CH_3NH_3PbI_3$ films do not show any noticeable position alterations i.e. the absorption onsets at 780 nm are very similar nevertheless, we observed a slight deviation in the absorption slopes which are below the band edge. Such deviations (without base line correction) could appear from strong light scattering, which originates from rough perovskite surface, rather than from the effect of additives. However, in order to verify whether presence of additive have any influence on the band gap position, we evaluated approximate band gap positions from the measured spectra. By performing scattering subtraction which is proportional to λ^{-4} and by applying extrapolation to the linear part of absorption edge, we obtained that optical band gap of all synthesized films to be around 1.58eV, which is in agreement with literature[32]. It should be noted that due to a very high perovskite layer thickness, which is ≈300 nm, absorption spectrum below 600 nm becomes saturated and therefore precise interpretation of the results in this region becomes difficult.

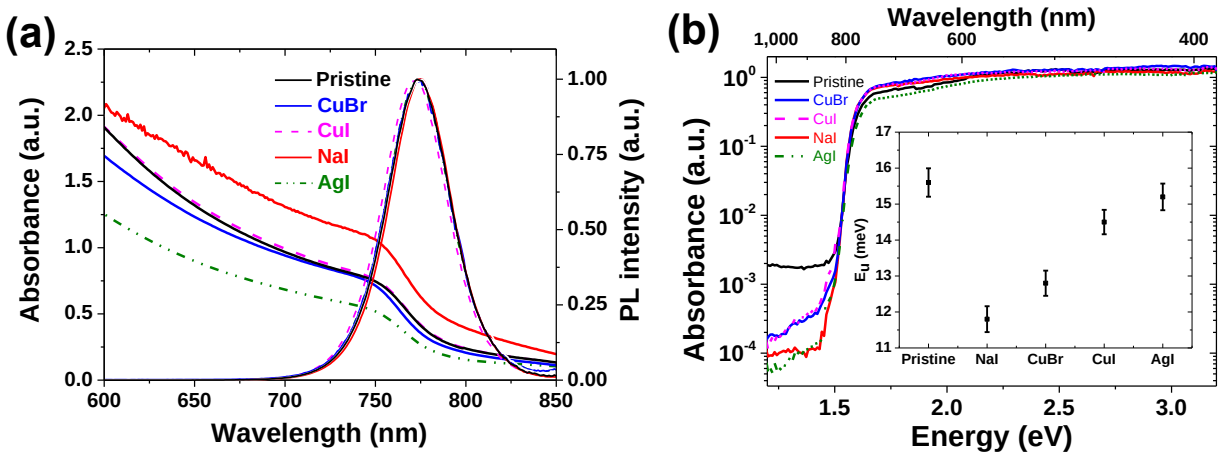

Figure 4. (a) Steady state absorption and PL spectra for pristine and additives based perovskite films. (b) The absorption spectra of perovskite films derived from pristine and additive based lead sources measured using the PDS technique. The inset shows the corresponding Urbach energies for all samples. The error bar is defined by the s.d in fitting the Urbach tail.

2.3.2. Photoluminescence study

Steady state PL spectra of perovskite films are presented in Figure 4a. Strong and narrow fluorescence bands with full-width half maximum of about 40 nm appear at around 775 nm upon sample excitation at 460 nm. It is observed that the PL spectra are similar for all $CH_3NH_3PbI_3$ films, i.e. pristine and additives based, confirming that the additives did not affect band edge of organo-metal perovskite semiconductors. This could be due to the tendency of additives to be at the crystalline surfaces rather than having impact on the band gap of perovskite films. Most likely, the effect of additives on the perovskite crystallization is more pronounced and influences film morphology which, can affect the photovoltaic performances[16]. PL decay measurements were performed using time-correlated single photon counting technique (see details in Figure S2). The estimated PL lifetimes and their relative contributions are summarized in Table S1. It is evident that PL decay kinetics experience several important differences depending on the type of additive.

2.4. Photothermal deflection spectroscopy (PDS)

We used photothermal deflection spectroscopy (PDS), which is an ultrasensitive absorption measurement technique, to explore the optical absorption of the $CH_3NH_3PbI_3$ films near the band edge (Figure 4b). PDS has a dynamic sensitivity range of 4-5 orders of magnitude and is less affected by optical light scattering. From Figure 4b, it is evident that the pristine perovskite has the highest sub-bandgap absorption. In addition, both copper based perovskite (e.g. CuI and CuBr) samples shows relatively higher absorption compared to the AgI and NaI based perovskite films in the sub-bandgap region. It is notable that Cu based additives create a tail in the absorption spectra of perovskite which confirm the presence of these monovalent cations inside the film. In contrast to AgI and NaI, copper based additives absorb intrinsically (Figure S3) which generate aforementioned tail. Comparing the PDS absorption spectra for CuBr based PbI_2 and perovskite shows that these additives are not fully incorporated in the perovskite film.

As reported by Sadhanala et al. for $CH_3NH_3PbI_3$, we observe sharp band edges for all the samples with an exponential decay of the density of states after the band edge, known as the Urbach tail[31,33]. The extent of the absorption tail below the band gap is correlated with the degree of electronic disorder within the material, which could originate from structural disorder, thermal fluctuation of the ions comprising the material and defects in the crystalline structure. Indeed, there have been several recent reports which suggest that the presence of defects within $CH_3NH_3PbI_3$ perovskite crystals would induce localized states in the range of a few hundred meV from the extended states of the bands, which could result in the broadening of the Urbach tail[34]. Assuming the same level of thermal disorder, the slope of the exponential part of the Urbach tail gives an estimation of the defect density, in terms of Urbach energy 'E_u'[31,33]. The estimated Urbach energies for the pristine and additive based perovskite samples are shown in the inset of Figure 4b, along with the respective fitting error, which are 15.6, 11.8, 12.8, 13.5 and 15.2 meV for pristine, NaI, CuBr, CuI and AgI based perovskite, respectively. The data fittings are shown in

the Figure S4. These values suggest that within the measurement error, additive based perovskite, particularly NaI, CuBr and CuI, have a lower level of electronic disorder compared to the pristine perovskites.

2.5. Kelvin probe force microscopy (KPFM)

We then used Kelvin probe force microscopy (KPFM), an electrical operation mode of scanning force microscopy (SFM), to investigate the effect of adding monovalent cation halide on $CH_3NH_3PbI_3$ perovskite Fermi level. KPFM is a powerful technique based on measuring and compensating the electrostatic forces between a sample and an AFM tip to determine the local contact potential difference (CPD)[35,36], which is a measure of the Fermi level energy if the electron affinity is known. Previously, it has been used to study the electrical potential distribution across the internal interfaces of inorganic solar cells[37,38]. KPFM was recently used to characterize the perovskite top layer[39,40], where the presence of a small potential barrier at the grain boundaries was found. Bergmann et al. have recently measured cross-sections of a complete perovskite based solar cell under illumination with KPFM and showed that the potential is similar to a p-i-n type junction[41]. Figure 5 shows CPD of line profiles recorded at pristine and additive based perovskite films which is sensitive to the surface work functions Φ of the materials. The line scan is carried out at the interface of perovskite and gold layer as shown in topography AFM image (Figure 5). Assuming that the tip work function remains constant during a line scan, the CPD reflects the built-in potential of the device. It is notable that adsorbed water on the surface may have altered the absolute value of the CPD, but not the relative difference between the studied materials.

We found a decreasing CPD from the pristine perovskite (0.3 V) towards the Au electrode (≈0V, black line profile in in Figure 5). The difference between these two values corresponds to the differences of the work function of perovskite ($\Phi_{perovskite}$ / e≈ 4.8 V) and Au (Φ_{Au}/e≈5.1 V) which

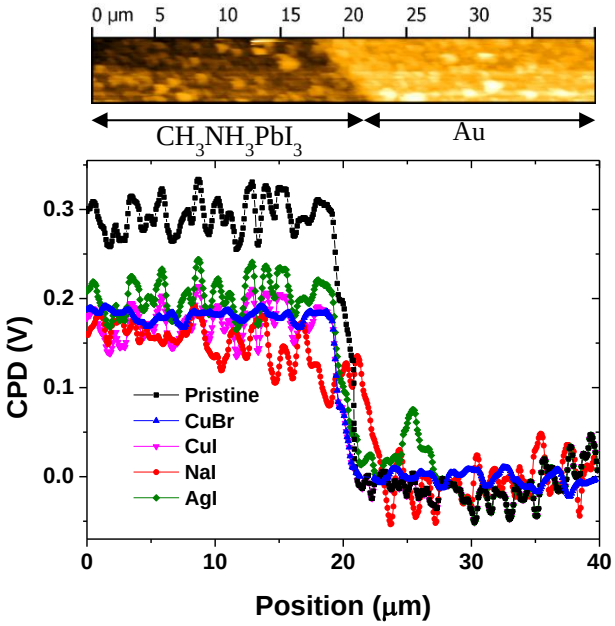

Figure 5. CPD line profiles recorded from pristine and additive based perovskite films using KPFM. The AFM topography image is shown on the top.

are comparable to the previous reports[41,42]. Surprisingly, the work function of additive based perovskite shifted significantly (about 0.1V) toward the Au work function. This shift in the work function can be attributed to the following two reasons; first, substitutional doping of perovskite in which Pb^{2+} is replaced by Cu^{+}, Na^{+} and Ag^{+} cations resulting in generation of valance band holes. Thus, the Fermi level of the bulk perovskite thin film comes closer to the valence band. Secondly, these additives can potentially passivate the surface of perovskite film (where there is a missing iodide) and as a result reduce the contact potential difference which is measured by KPFM. It is notable that the chance of substitutional doping at the room temperature is very low since the excess energy associate with putting these monovalent cation (e.g. Ag^{+}) in place of Pb^{2+} is very high[43]. Thus, the second scenario is more probable in which the crystalline surfaces of $CH_3NH_3PbI_3$ are passivated in the presence of these monovalent cations.

2.6. Charge transport measurement

To further understand the role of the monovalent cations on the properties of the perovskite material, extensive charge transport measurements were performed. Both electron and hole only devices were fabricated (see details in Experimental section) with all the different perovskite materials to estimate the bulk carrier mobility (μ_{SCL}). A clear transition from the linear to space charge limited trap free behavior is observed in all the materials (Figure 6a). The onset voltage of the trap-free space charge limited (TFSCL) transport regime is directly related to the density of trap states at the transport level[44]. In general, all the perovskite devices with typical thickness in the range of 0.5 - 1 μm demonstrated TFSCL in a voltage range of < 5V, indicating low trap density. Child's law given by: $J = \frac{9}{8}\,\varepsilon_0\epsilon_r\mu_{SCL}\frac{V^2}{d^3}$ where, J is the current density, ε_o is the vacuum permittivity, ε_r is the dielectric constant of the active material which is measured to be in the range of 15 - 25 (at 1 kHz) for different materials and d is the thickness of the active layer was utilized to estimate the bulk mobility of electrons and holes in the TFSCL regime[45].

Typical electron mobility (μ_{SCL}^{e}) of 0.02 $cm^2.V^{-1}.s^{-1}$ and hole mobility (μ_{SCL}^{h}) of 0.008 $cm^2.V^{-1}.s^{-1}$ was obtained for pristine perovskite films. This magnitude of bulk mobility is lower than that reported for a single crystal of perovskite[44]. It should be noted that hysteresis was observed in the J-V measurements and hence for a conservative estimate of the μ_{SCL}, forward sweep is considered. Moreover, factors like injection limited behavior have to be carefully considered to obtain the actual magnitude of μ_{SCL} in thin films. For TFSCL behavior, $J(E) \propto d^{-3}$, hence devices were also fabricated with different thickness to confirm the TFSCL behavior compared to injection limited behavior. As evident from Figure S5, J(E) decreases with increased thickness for the perovskite films.

Nevertheless, under similar conditions upon addition of the monovalent cation additive, the μ_{SCL} increased significantly (up to an order of magnitude) for holes compared to that for electrons. Hole mobility as high as 0.07 $cm^2.V^{-1}.s^{-1}$ was obtained for NaI based perovskite thin films (Figure

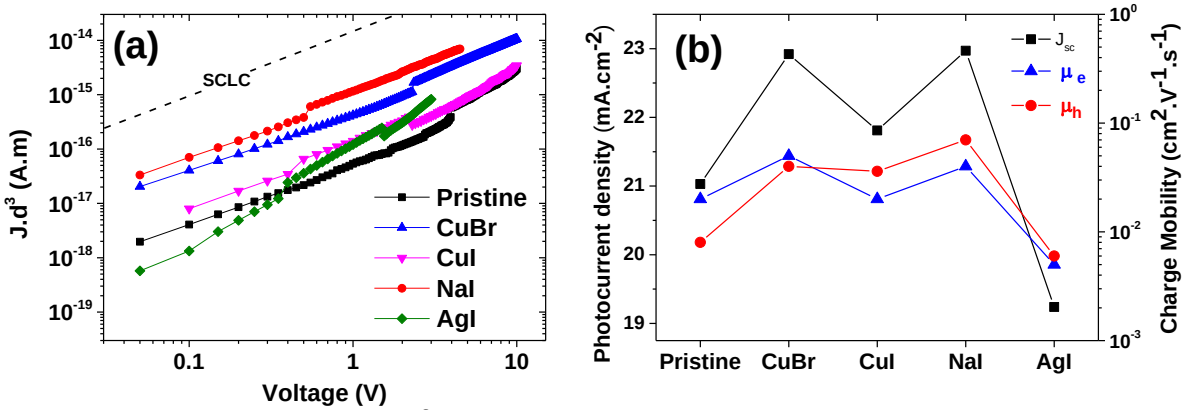

Figure 6. (a) J-V characteristics of hole only devices (ITO/PEDOT:PSS/Perovskite/Au), utilized for estimating the SCLC hole mobility. Note that the current density (J) is scaled with thickness of perovskite layers. (b) The trends in the J_{sc}, μ_h and μ_e for pristine and additive based perovskite.

6b). However, electron mobility increased to around 0.04 cm^2/Vs resulting in a more balanced charge transport. It should be noted that these values of bulk mobility are one of the highest in the community for perovskite thin films. Correspondingly, the conductivity magnitude estimated from the linear regime were obtained to be as high as 5×10^{-8} $S.cm^{-1}$ for NaI based perovskite compared to 10^{-9} $S.cm^{-1}$ for pristine films. It is evident from the charge transport measurements that the addition of monovalent cations strongly affect the balanced charge transport properties and the overall conductivity which is enhance the J_{sc} of the solar cells (Figure 6b). Thus it can be concluded that one of the strategies to increase the J_{sc} in perovskite solar cells could be to increase the balance between the bulk electron and hole transport.

To further understand the reason for the increased μ_{SCL}^{h} in additive based perovskite films, temperature dependent bulk transport measurements were performed. Arrhenius fits were utilized to estimate the activation energy (E_A) for the charge transport (Table 1). Adding of monovalent cations in the perovskite films results in a decrease of E_A for hole transport from 198 meV to 137 meV and electron transport from 13 meV to 77 meV. In the framework of a mobility edge model, it is expected that the increase in carrier concentration due to doping can result in filling up of the

traps at the transport level and decrease the barrier for transport which can diminish the activation energy. This is consistent with the observed change in the Fermi level of perovskite upon the addition of monovalent cation halide additives. Hence, it is plausible that the presence of stable +1 oxidation states of the cations results in passivation of traps in the system. Thus, it can be concluded from the charge transport measurements that the addition of monovalent cation halide additive results in enhancing the overall mobility of the charge carriers which is expected to enhance the J_{sc} of the perovskite solar cell devices.

2.7. Photovoltaic performance

Current density-voltage (J–V) characteristics of the pristine and additive based perovskite solar cells were measured under simulated air mass 1.5 global (AM1.5G) solar irradiation. The devices were fabricated based on the optimized procedure which is explained in the experimental section. A typical device has the structure of FTO/compact TiO_2/mesoporous TiO_2/$CH_3NH_3PbI_3$/Spiro-MeOTAD/Au, shown in Figure S7.

The influence of additive concentration on the photovoltaic performance of PSC was demonstrated by examining three different concentrations of CuBr (0. 01, 0.02 and 0.04 $mol.L^{-1}$) additive based perovskite devices (Figure S6). As summarized in Table S2, the lowest concentration slightly increased photocurrent density (J_{sc}) by 0.5 $mA.cm^{-2}$. By increasing the concentration of CuBr to 0.02 $mol.L^{-1}$ photovoltaic performance of the device revealed an average PCE of 15.4% while further increase in the amount of additive decreases J_{sc} and open circuit voltage (V_{oc}) which eventually brought down the overall power conversion efficiency (PCE) of the device. Therefore a concentration of 0.02 $mol.L^{-1}$ can be stated as the optimum level of the additive to realize the high performance of PSC.

Figure 7a and Table 1 show the influence of different additives on the photovoltaic parameters of

Table 1. Summary of the photovoltaic parameters derived from J-V measurements and charge mobilities along with activation energy for the pristine and additive based perovskite solar cells (showing the best performance) fabricated using two-step deposition method.

Type of Sample	J_{SC} (mA cm^{-2})	V_{OC} (V)	FF	PCE (%)	μ_e (cm^2/Vs)	μ_h (cm^2/Vs)	E_A^e (meV)	E_A^h (meV)
Pristine	21.03	0.95	0.70	14.01	0.02	0.008	135	198
CuBr	22.92	0.95	0.72	15.61	0.05	0.040	88	132
CuI	21.81	0.99	0.71	15.25	0.02	0.036	94	157
NaI	22.97	0.90	0.73	15.14	0.04	0.070	77	137
AgI	19.24	1.02	0.72	14.18	0.005	0.006	105	177

the PSC. It is notable that the statistics of the photovoltaic parameters follow the same trend as the best performing devices (Table S3). For the additive-free reference cell, J_{sc} of 21.03 mA.cm^{-2}, V_{oc} of 0.95 V, fill factor (FF) of 0.70 and PCE of 14.01% are achieved. The J_{sc} of AgI based device dropped nearly by 2 mA.cm^{-2} compare to the pristine cell which could be attributed to the lower loading of $CH_3NH_3PbI_3$ in AgI based sample (as it shows the lowest absorption in Figure 4b). On the other hand, because of the ideal surface coverage of AgI based perovskite, high V_{OC} of 1.02 V is achieved (Figure 1e). In addition, since the fill factor of AgI based device improved due to the relatively balanced charge transport (Figure 6a and Table 1), the overall efficiency of the device slightly improved to 14.18%.

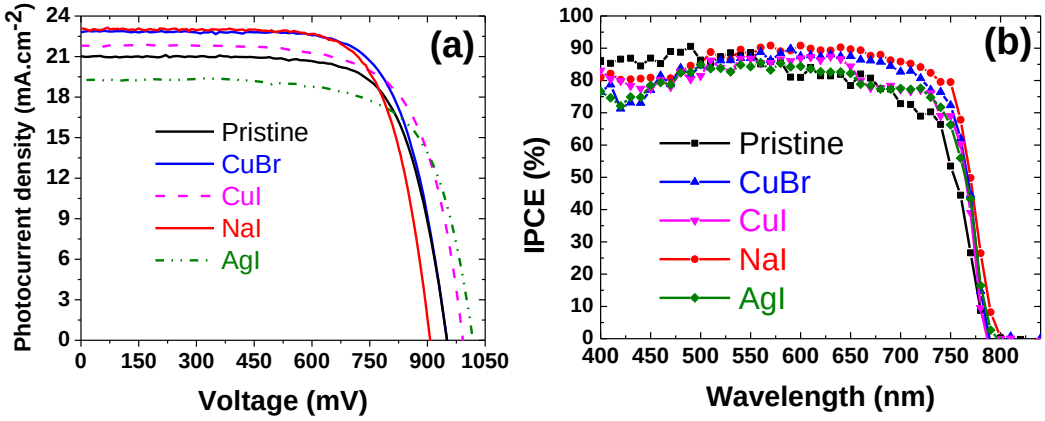

Figure 7. (a) Current-voltage characteristics of devices under illumination of 100 mW cm^{-2} obtained using different type of monovalent cation halide added to the lead source solution. (b) Incident photon-to-current efficiency (IPCE) spectra as a function of the wavelength of monochromatic light for the pristine, CuBr-, CuI-, NaI- and AgI-based perovskite solar cells.

Surprisingly, all other additives including NaI, CuBr and CuI enhanced the PCE of PSC notably to 15.14%, 15.61% and 15.25%, respectively. The open-circuit voltage of CuBr based device (0.95 V) was similar to that of pristine one while a considerable drop of around 50mV is noticed for NaI based cells (0.90 V). The lower voltage in NaI based derived samples can be explained due to the presence of increased shunting pathways because of detrimental contact between spiro-OMeTAD and mesoporous TiO_2 layer which is quite expected from a rougher perovskite films, (SEM images in Figure 1d). In contrast, a uniform and pinhole free surface of CuI based $CH_3NH_3PbI_3$ sample lead to the improvement in V_{oc} (0.99 V vs 0.95 V for additive-free reference) (Figure 1c).

Moreover, a substantial enhancement in the J_{sc} of 21.81 $mA.cm^{-2}$ for CuI, 22.92 $mA.cm^{-2}$ for CuBr and 22.97 $mA.cm^{-2}$ for NaI based devices compared to 21.03

$mA.cm^{-2}$ for pristine solar cells was observed. The highest J_{sc} exhibited by NaI based device can be attributed to the better conversion of PbI_2 into $CH_3NH_3PbI_3$ as revealed by XRD pattern (Figure 3) and therefore higher loading of perovskite inside the meso-TiO_2 scaffold which is consistent with the PDS data (Figure 4b). However, diminished photocurrent density observed in other samples, i.e., AgI could be attributed to the relatively low conversion of lead halide into $CH_3NH_3PbI_3$ under given conditions. The enhancement in current densities of PSC based on NaI, CuBr and CuI-based $CH_3NH_3PbI_3$ are supported by the improvement in the incident photon to current conversion efficiency (IPCE) spectra shown in Figure 7b. In addition, IPCE of all the devices as a function of wavelength shows that the generation of photocurrent starts at around 780 nm, which is in agreement with the band edge of pristine $CH_3NH_3PbI_3$. This confirms further that the presence of additives does not change the band gap of the perovskite material which is consistent with PDS results. We also noticed that the fill factors (FFs) of devices based on the NaI and CuBr based perovskite improved noticeably, in comparison with the pristine reference cell. Arguably, improvement of FFs could be due to the enhancement in conductivity and presence of lower level of electronic disorder in the additive based $CH_3NH_3PbI_3$ films (Figure 4b, 6 and Table 1).

3. Conclusions

In summary, we have systematically studied the role of the monovalent cation halide based additives on the morphological, optical and electrical properties of $CH_3NH_3PbI_3$ perovskite films. We found that a better conversion of lead iodide into $CH_3NH_3PbI_3$ structure is achieved for NaI and CuBr based films which was confirmed by XRD and, for CuI and AgI based perovskite a uniform film with a continuous coverage is formed. Detailed experiments based on PDS, KPFM and bulk transport measurements on the

pristine and additive based perovskites indicate that the additives can possibility cause a passivation of states at the crystallite surfaces. This minimizes the extrinsic doping at the crystallite boundaries and improves the overall charge transport properties as well as the solar cell performance. These observations indicate that the additives seem to passivate the hole traps in the surface (or grain boundaries) of perovskite films that results in an enhancement of J_{sc} and hence, the overall efficiency of the solar cell. The confluence of aforementioned favourable properties led to the enhancement of PCE to 15.14%, 15.25% and 15.61% for NaI, CuI and CuBr, respectively, in comparison with 14.01% for the additive-free reference cell. The photovoltaic results, particularly for AgI based cell, confirm that the ideal surface coverage of perovskite is not the only sufficient factor to achieve a high efficiency but also a full conversion of lead iodide into the perovskite is required. In summary, this work demonstrates the possibility of enhancing the structural and optoelectronic properties that play a very crucial role in improving the performance of perovskite based solar cells by simple addition of a rational amount of low cost monovalent cation based inorganic salts.

4. Experimental Section

Materials. Unless stated otherwise, all materials were purchased from Sigma- Aldrich or Acros Organics and used as received. Spiro-MeOTAD was purchased from Merck KGaA. CH_3NH_3I was synthesized according to a reported procedure[3].

Photoanode preparation. Devices were fabricated on laser patterned FTO-coated glass (NSG 10, Nippon sheet glass, Japan). Initially, FTO substrates were cleaned sequentially in 2% Hellmanex detergent, 2-propanol and ethanol, and then treated with a ultraviolet/O_3 cleaner for 15 min. A hole-blocking layer of compact TiO_2 was deposited by spray pyrolysis using a precursor solution of titanium di-isopropoxide bis(acetylacetonate; 0.6 ml titanium acetylacetonate in 8ml ethanol) on a hot plate at

450 ^{o}C. The titanium acetylacetonate was prepared by pouring acetylacetone (Wako Pure Chemical Industries, Ltd.) into titanium isopropoxide (Kanto Chemical Co., Inc.) with a mole ratio of 2:1. For the preparation of mesoporous TiO_2 scaffold, a commercial TiO_2 paste (Dyesol 30NRD) was diluted with ethanol (2:7, weight ratio) and was then deposited by spin coating at 5,000 r.p.m. for 30 s. After drying at 125 ^{o}C, the TiO_2 films were gradually heated to 500 ^{o}C and annealed at this temperature for 20 min.

Synthesis and deposition of pristine and additive based $CH_3NH_3PbI_3$. PbI_2 was dissolved in N,N-dimethylformamide (DMF) at a concentration of 1.2M under constant stirring at 80 ^{o}C. The halide salts including NaI, CuBr, CuI and AgI were then added to the lead halide solution at a concentration of 0.02M. All the solution were prepared inside an argon glove box under moisture- and oxygen-controlled conditions (H_2O level: <1 ppm and O_2 level: <10 ppm). The $CH_3NH_3PbI_3$ films were prepared using two-step deposition method[6]. In the first step, the mesoporous TiO_2 was infiltrated with pure or additive based PbI_2 solution by spin coating at 6500 rpm for 30 s and dried at 80 ^{o}C for 30 min., To form perovskite resulting PbI_2 films were dipped in a solution of CH_3NH_3I in 2-propanol (8 mg mL^{-1}) for 30 s, and were dried at 80 °C for 30 min after cooling to room temperature

Solar cells fabrication. After infiltration of TiO_2 scaffold with pure and additive based $CH_3NH_3PbI_3$, the hole transport material (HTM) was deposited by spin coating at 4,000 rpm for 30 s. The spin coating formulation of HTM was prepared by dissolving 72.3 mg spiro-MeOTAD, 28.8 ml 4-tert-butylpyridine, 17.5 ml of a stock solution of 520 mgml^{-1} lithium bis (trifluoromethylsulphonyl) imide in acetonitrile and 29 ml of a stock solution of 300 mgml^{-1} tris(2-(1H-pyrazol-1-yl)-4-tert-butylpyridine) cobalt(III) bis (trifluoromethyl sulphonyl) imide in acetonitrile in 1 ml chlorobenzene. Finally,

70nm of gold was thermally evaporated on top of the device to form the back contact. The device fabrication was carried out under controlled atmospheric conditions with a humidity of <1%.

Material characterization. Field-emission scanning electron microscope (FESEM, Merlin) was employed to examine morphology of the pristine and additive based perovskite films. An electron beam accelerated to 3 kV was used with an in-lens detector**.** The atomic force microscope (AFM) images were obtained using a Thermo Microscope M5 in non-contact mode and scanning over a range of 15 μm by 15μm at a resolution of 256×256 data points. The surface roughness was measured as the root mean-squared roughness over the scanning area. 2θ scans were obtained from samples of perovskite deposited on the mesoporous TiO_2-coated FTO glass using Bruker Advance D8 X-ray diffractometer with a graphite monochromator, using Cu-K_α radiation, at a scanning rate of 0.5 deg.min^{-1}. X-ray photoelectron spectroscopy (XPS) was performed on an X-ray photoelectron spectrometer (ESCALAB 250Xi, Thermo Fisher SCIENTIFIC INC., USA) with Al Kα radiation(hν= 1486.6 eV) as the source.

Optical characterization. The steady state optical properties of perovskite films were studied using UV-visible absorption and fluorescence spectroscopy. The absorption spectra of perovskite films were recorded with convenient UV-Vis-NIR spectrophotometer (CARY-5) in transmission mode. Fluorescence spectra and fluorescence decay kinetics were recorded on a spectrofluorometer Fluorolog 322. Fluorescence spectra were recorded by exciting the samples with 450 W Xenon lamp at a fixed wavelength of 460 nm and scanning the emission monochromator from 500 to 850 nm. Same spectrometer working in a single-photon counting mode was used for the measurements of fluorescence decay kinetics with sub-nanosecond time resolution. Picosecond pulsed diode laser head NanoLED-405LH (Horiba) emitting <200 ps

duration pulses at 406 nm with repetition rate of 1 MHz and pulse energy about 11 pJ was use as an excitation source.

Photothermal deflection spectroscopy (PDS). PDS as a scatter-free surface sensitive absorption measurement were performed on the pristine and additive based perovskite films. Samples prepared in an identical fashion to the solar cell preparation were spun onto spectrosil quartz slides (which were cleaned with acetone, isopropanol, and water followed by a 10 min oxygen plasma etch). For this particular measurement, we made use of quartz rather than the FTO-coated glass to minimize light absorption by the substrate. During the measurement we kept the samples in a hermetically sealed quartz cuvette filled with an inert liquid, Fluorinert FC-72 from 3M Corporation, which acts as the deflection medium with high temperature dependent refractive index. We excited the perovskite films with a modulated monochromated light beam perpendicular to the plane of the sample. A modulated monochromated light beam was produced by a combination of a Light Support MKII 100W Xenon arc source and a CVI DK240 monochromator. The transverse probe beam was produced with Qioptiq 670-nm fibre-coupled diode laser and passed as close as possible to the perovskite film surface. Beam deflection was measured using a differentially amplified quadrant photodiode and a Stanford Research SR830 lock-in amplifier which is proportional to the absorption in the sample.

Kelvin probe measurement. Our KPFM apparatus is a Veeco Dimension 3100 system operated in ambient atmosphere. This system was selected due to its ability of scanning over a length of 80 μm. The PtIr tip (Bruker, SCM-PIT, 60-100k Hz), which has a work function of about 4.85 eV was used for this measurement. The oscillation of the tip is controlled in an amplitude-modulation (AM) mode.

Diode for SCLC measurement. Devices were fabricated on pre-cleaned ITO substrates (15 ohm.Sq^{-1}), obtained from XINYAN Technology Ltd. For hole only devices (ITO/PEDOT:PSS/Perovskite/Au), PEDOT:PSS was spin coated at 2000 rpm and annealed at 180^0C for 1 hour in air. Perovskite films both pristine and doped were obtained by a two-step deposition process as described earlier to obtain films of thickness 0.5 - 1 μm. Similarly electron only devices (ITO/Perovskite/PCBM/Al) were fabricated. Thin PCBM layer of around 20- 30 nm was utilized to prevent the degradation of the Al electrode due to the perovskite. It was ensured that the presence of a thin layer of PCBM does not significantly degrade the electron transport of the perovskite. Metal electrodes were coated by thermal evaporation (10^{-6} mbar, 0.1 A^0/s, 60 nm thick). The devices were characterized using Keithley 4200 SCS and temperature was varied using a RF probe station from Cryogenic Technologies.

Solar cell characterization. Current–voltage characteristics were recorded by applying an external potential bias to the cell while recording the generated photocurrent with a digital source meter (Keithley Model 2400). The light source was a 450-W xenon lamp (Oriel) equippedwith a Schott-K113 Tempax sunlight filter (Praezisions Glas & OptikGmbH) to match the emission spectrum of the lamp to theAM1.5G standard. Before each measurement, the exact light intensity was determined using a calibrated Si reference diode equipped with an infrared cut-off filter (KG-3, Schott). IPCE spectra were recorded as a function of wavelength under a constant white light bias of approximately 5mWcm^{-2} supplied by an array of white light emitting diodes. The excitation beam coming from a 300-W xenon lamp (ILC Technology) was focused through a Gemini-180 double monochromator (Jobin Yvon Ltd) and chopped at approximately 2 Hz. The signal was recorded using a Model SR830 DSP Lock-In Amplifier (Stanford Research Systems). All measurements were

conducted using a non-reflective metal aperture of 0.159 cm^2 to define the active area of the device and avoid light scattering through the sides.

The data underlying this paper are available at https://www.repository.cam.ac.uk/handle/1810/254105.

Supporting Information

Macroscopic pictures, lifetime measurement, PDS spectra of PbI_2 and perovskite, data fittings of Urbach energy, thickness dependency of charge mobility measurement, current-voltage curves and table containing the photovoltaic parameters derived from JV curves obtained from a batch of devices, SEM cross sectional micrographs of a complete device, thickness measurement by profilometer, FWHM values from the XRD patterns, forward and reverse JV scans, normalized PCE of devices as function of time and XPS measurement are provided in in Supporting Information which is available from the Wiley Online Library or from the author.

Acknowledgements

M.A.J. thanks Nyak Technology Limited for a PhD scholarship. R.H.F, M.A.J., and A.S. would like to acknowledge the support from EPSRC. M.I.D., S.M.Z., and M.G. thank the King Abdulaziz City for Science and Technology (KACST) and Swiss National Science Foundation (SNSF) for financial support. N.A. gratefully acknowledges financial support from the Swiss confederation under Swiss Government Scholarship program. The authors would like to thank Dr. Pierre Mettraux in Molecular and Hybrid Materials Characterization Center, EPFL for carrying out XPS measurements. A.S. gratefully acknowledges financial support from the Indo-UK APEX project. S.P.S. acknowledges Royal Scociety London for the Newton Fellowship.

[1] A. Kojima, K. Teshima, Y. Shirai, T. Miyasaka, *J. Am. Chem. Soc.* **2009**, *131*, 6050.

[2] H.-S. Kim, C.-R. Lee, J.-H. Im, K.-B. Lee, T. Moehl, A. Marchioro, S.-J. Moon, R. Humphry-Baker, J.-H. Yum, J. E. Moser, M. Grätzel, N.-G. Park, *Sci. Rep.* **2012**, *2*, 591.

[3] D. Liu, T. L. Kelly, *Nat. Photonics* **2013**, *8*, 133.

[4] Q. Dong, Y. Fang, Y. Shao, P. Mulligan, J. Qiu, L. Cao, J. Huang, *Science* **2015**, 347, 967–970.

[5] J. H. Noh, S. H. Im, J. H. Heo, T. N. Mandal, S. Il Seok, *Nano Lett.* **2013**, *13*, 1764.

[6] J. Burschka, N. Pellet, S.-J. J. Moon, R. Humphry-Baker, P. Gao, M. K. Nazeeruddin, M. Grätzel, M. Gratzel, *Nature* **2013**, *499*, 316.

[7] M. Grätzel, S. Seok, *Nat. Photonics* **2013**, *7*.

[8] M. M. Lee, J. Teuscher, T. Miyasaka, T. N. Murakami, H. J. Snaith, *Science* **2012**, 338, *643–647.*

[9] M. Liu, M. B. Johnston, H. J. Snaith, *Nature* **2013**, *501*, 395.

[10] W. S. Yang, J. H. Noh, N. J. Jeon, Y. C. Kim, S. Ryu, J. Seo, S. Il Seok, *Science,* **2015**, 12, *1234-1237.*

[11] B. Nicholson, S. Verma, P. Med, *Science* **2015**, 345, 542-546.

[12] N. J. Jeon, J. H. Noh, W. S. Yang, Y. C. Kim, S. Ryu, J. Seo, S. Il Seok, *Nature* **2014**, *517*, 476.

[13] Y. Zhou, M. Yang, W. Wu, A. L. Vasiliev, K. Zhu, N. P. Padture, *J. Mater. Chem. A* **2015**, *3*, 8178.

[14] M. A. Green, A. Ho-Baillie, H. J. Snaith, *Nat. Photonics* **2014**, *8*, 506.

[15] M. J. Carnie, C. Charbonneau, M. L. Davies, J. Troughton, T. M. Watson, K. Wojciechowski, H. Snaith, D. a Worsley, *Chem. Commun. (Camb).* **2013**, *49*, 7893.

[16] J.-H. Im, I.-H. Jang, N. Pellet, M. Grätzel, N.-G. Park, *Nat. Nanotechnol.* **2014**, *9*, 927.

[17] Z. Cheng, J. Lin, *CrystEngComm* **2010**, *12*, 2646.

[18] W. Nie, H. Tsai, R. Asadpour, J. Blancon, A. J. Neukirch, G. Gupta, J. J. Crochet, M. Chhowalla, S. Tretiak, M. A. Alam, H. Wang, A. D. Mohite, *Science* **2015**, 347, 522-525.

[19] S. D. Stranks, G. E. Eperon, G. Grancini, C. Menelaou, M. J. P. Alcocer, T. Leijtens, L. M. Herz, A. Petrozza, H. J. Snaith, *Science* **2013**, 342, 341–345.

[20] W. Zhang, M. Saliba, D. T. Moore, S. K. Pathak, M. T. Ho, T. Stergiopoulos, S. D. Stranks, G. E. Eperon, J. A. Alexander-webber, A. Abate, A. Sadhanala, S. Yao, Y. Chen, R. H. Friend, L. A. Estroff, U. Wiesner, H. J. Snaith, *Nat. Commun.*, **2015**, 6, *7142*.

[21] J. Navas, A. Sanchez-Coronilla, J. J. Gallardo, N. Cruz Hernández, J. C. Pinero, R. Alcántara, C. Fernández-Lorenzo, D. M. de los Santos, T. Aguilar, J. Martín-Calleja, *Nanoscale* **2015**,7, 6216-6229.

[22] N. Pellet, P. Gao, G. Gregori, T. Y. Yang, M. K. Nazeeruddin, J. Maier, M. Grätzel, *Angew. Chemie - Int. Ed.* **2014**, *53*, 3151.

[23] Y. Ogomi, A. Morita, S. Tsukamoto, T. Saitho, N. Fujikawa, Q. Shen, T. Toyoda, K. Yoshino, S. S. Pandey, S. Hayase, *J. Phys. Chem. Lett.* **2014**, 5 (6), 1004–1011.

[24] F. Hao, C. C. Stoumpos, R. P. H. Chang, M. G. Kanatzidis, *J. Am. Chem. Soc.* **2014**, *136*, 8094.

[25] Y. Zhou, M. Yang, A. L. Vasiliev, H. F. Garces, *J. Mater. Chem. A Mater. energy Sustain.* **2015**, *00*, 1.

[26] M. I. Dar, N. Arora, P. Gao, S. Ahmad, M. Gratzel, M. K. Nazeerudding, *J. Phys. Chem. Lett.* **2014**, 5 (6), 1004–1011.

[27] K. Liang, D. Mitzi, M. Prikas, *Chem. Mater.* **1998**, *4756*, 403.

[28] G. Niu, X. Guo, L. Wang, *J. Mater. Chem. A* **2015**, Advance.

[29] T. Baikie, Y. Fang, J. M. Kadro, M. Schreyer, F. Wei, S. G. Mhaisalkar, M. Gratzel, T. J. White, *J. Mater. Chem. A* **2013**, *1*, 5628.

[30] a. L. Patterson, *Phys. Rev.* **1939**, *56*, 978.

[31] S. De Wolf, J. Holovsky, S.-J. Moon, P. Löper, B. Niesen, M. Ledinsky, F.-J. Haug, J. Yum, C. Ballif, S. De Wolf, *J. Phys. Chem. Lett.* **2014**, 5, 1035-1039.

[32] C. Wehrenfennig, M. Liu, H. J. Snaith, M. B. Johnston, L. M. Herz, *J. Phys. Chem. Lett.* **2014**, *5*, 1300.

[33] A. Sadhanala, F. Deschler, T. H. Thomas, E. Dutton, K. C. Goedel, F. C. Hanusch, M. L. Lai, U. Steiner, T. Bein, P. Docampo, D. Cahen, R. H. Friend, *J. Phys. Chem. Lett.* **2014**, 5 (15), 2501–2505.

[34] J. Kim, S. H. Lee, J. H. Lee, K. H. Hong, *J. Phys. Chem. Lett.* **2014**, *5*, 1312.

[35] M. Nonnenmacher, M. P. O'Boyle, H. K. Wickramasinghe, *Appl. Phys. Lett.* **1991**, *58*, 2921.

[36] G. Elias, T. Glatzel, E. Meyer, A. Schwarzman, A. Boag, Y. Rosenwaks, *Beilstein J. Nanotechnol.* **2011**, *2*, 252.

[37] I. Visoly-Fisher, S. R. Cohen, D. Cahen, C. S. Ferekides, *Appl. Phys. Lett.* **2003**, *83*, 4924.

[38] C. S. Jiang, F. S. Hasoon, H. R. Moutinho, H. a. Al-Thani, M. J. Romero, M. M. Al-Jassim, *Appl. Phys. Lett.* **2003**, *82*, 127.

[39] E. Edri, S. Kirmayer, A. Henning, S. Mukhopadhyay, K. Gartsman, Y. Rosenwaks, G. Hodes, D. Cahen, *Nano Lett.* **2014**, *14*, 1000.

[40] P. Qin, A. L. Domanski, A. K. Chandiran, R. Berger, H.-J. Butt, M. I. Dar, T. Moehl, N. Tetreault, P. Gao, S. Ahmad, M. K. Nazeeruddin, M. Grätzel, *Nanoscale* **2014**, *6*, 1508.

[41] V. W. Bergmann, S. a. L. Weber, F. Javier Ramos, M. K. Nazeeruddin, M. Grätzel, D. Li, A. L. Domanski, I. Lieberwirth, S. Ahmad, R. Berger, *Nat. Commun.* **2014**, *5*, 5001.

[42] A. Dymshits, A. Henning, G. Segev, Y. Rosenwaks, L. Etgar, *Sci. Rep.* **2015**, *5*, 8704.

[43] M. Cargnello, A. C. Johnston-Peck, B. T. Diroll, E. Wong, B. Datta, D. Damodhar, V. V. T. Doan-Nguyen, A. a. Herzing, C. R. Kagan, C. B. Murray, *Nature* **2015**, *524*, 450.

[44] D. Shi, V. Adinolfi, R. Comin, M. Yuan, E. Alarousu, A. Buin, Y. Chen, S. Hoogland, A. Rothenberger, K. Katsiev, Y. Losovyj, X. Zhang, P. A. Dowben, O. F. Mohammed, E. H. Sargent, O. M. Bakr, *Science* **2015**, 347, 519–522.

[45] S. P. Senanayak, a Z. Ashar, C. Kanimozhi, S. Patil, K. S. Narayan, *Phys. Rev. B*, **2015**, 91, 115302.

The table of contents entry

Incorporation of monovalent cation halide additives improve the semiconductor behaviour and photovoltaic performance of $CH_3NH_3PbI_3$ perovskite through formation of uniform and continuous perovskite film, better conversion and loading of $CH_3NH_3PbI_3$ and possible passivation of defects states at the crystallite surfaces as well as the enhancement in the bulk charge transport along with a minimization of disorder.

Keywords: Monovalent cation halide, additives, $CH_3NH_3PbI_3$ Perovskite, doping, surface passivation

Mojtaba Abdi-Jalebi, M. Ibrahim Dar, Aditya Sadhanala, Satyaprasad P. Senanayak, Marius Franckevičius, Neha Arora, Yuanyuan Hu, Mohammad Khaja Nazeeruddin, Shaik M. Zakeeruddin, Michael Grätzel,* Richard H. Friend**

Impact of monovalent cation halide additives on the structural and optoelectronic properties of $CH_3NH_3PbI_3$ perovskite

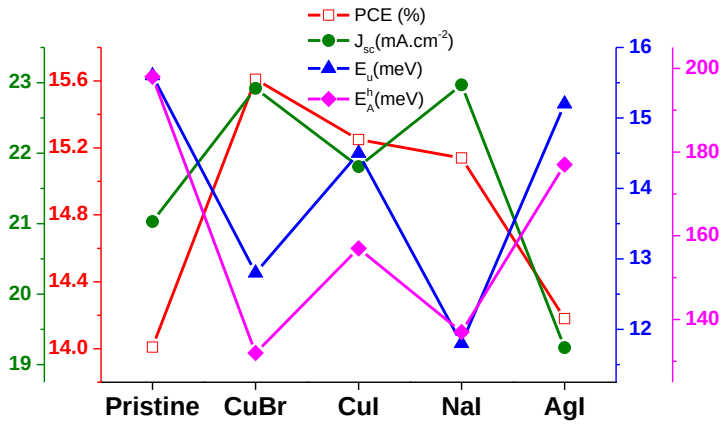

Supporting Information

Impact of monovalent cation halide additives on the structural and optoelectronic properties of $CH_3NH_3PbI_3$ perovskite

Mojtaba Abdi-Jalebi, Mohammad Ibrahim Dar, Aditya Sadhanala, Satyaprasad P. Senanayak, Marius Franckevičius, Neha Arora, Yuanyuan Hu, Shaik Mohammad Zakeeruddin, Mohammad Khaja Nazeeruddin, Michael Grätzel,* Richard H. Friend**

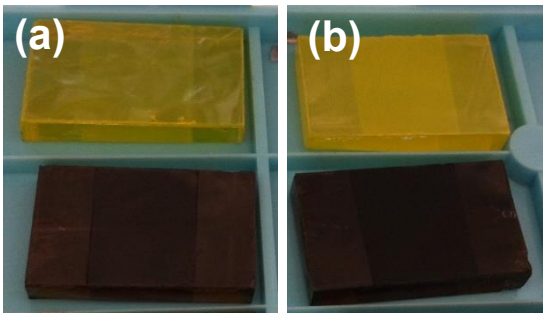

Figure S1. Macroscopic pictures of PbI_2 (top) and $CH_3NH_3PbI_3$ (bottom) films for (a) pristine and (b) NaI-based samples.

Lifetime measurements

Although the addition of additive does not modify the bandgap of $CH_3NH_3PbI_3$ perovskite, the presence of low amount of additives can influence free or bound carrier dynamics. To estimate the charge carrier lifetimes, we performed photoluminescence lifetime measurements using time-correlated single photon counting. Photoluminescence decay kinetics of perovskite films deposited on mesoporous TiO_2 in the absence of hole transport materials (HTM) are shown in Fig. 4b. PL traces for all investigated samples can be approximated by exponential functions containing two time constants. The estimated PL lifetimes and their relative contributions are summarized in Table S1. It is evident that PL decay kinetics experience several important differences depending on the type of additive. In comparison to pristine sample a fast PL decay component becomes slightly slower whereas long lived decay becomes accelerated in additive based samples. Moreover, the contribution

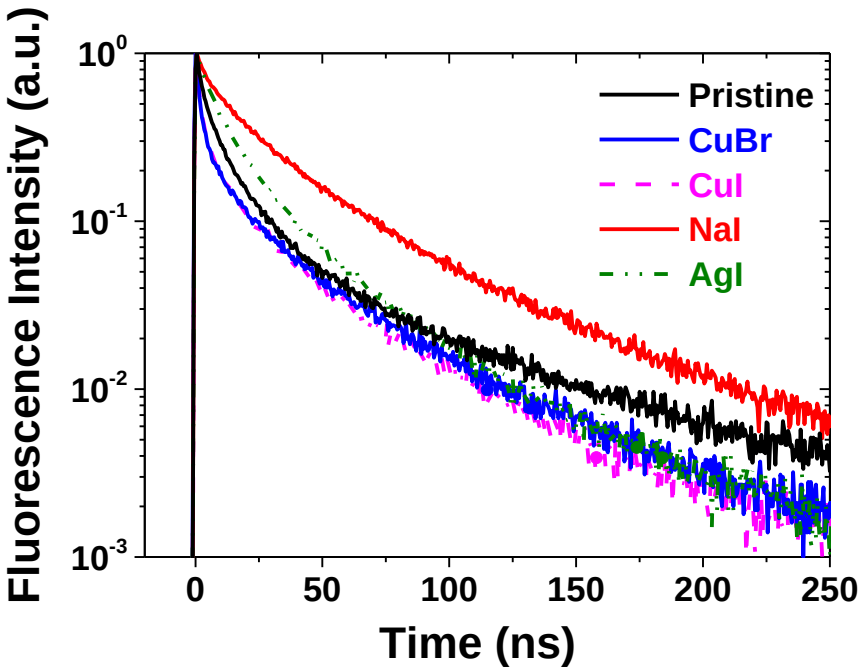

Figure S2. Fluorescence decay kinetics measured at 780 nm upon excitation at 406 nm with fluence of 11 $pJ.cm^{-2}$ for pristine and additives based perovskite films.

of τ_1 relaxation components became slightly higher (>50 %) upon addition of silver and sodium iodides, whereas its contribution decreases significantly for copper halide based samples. These observations can have implications in the recombination processes and disorder dynamics. However, a detailed analysis of these is beyond the scope of this work.

Table S1. The summarized emission lifetime "τ" and corresponding intensities "A" for various perovskite samples obtained using three exponential fit.

	Ref	**CuI**	**CuBr**	**NaI**	**AgI**
A_1, %	32.6	18.2	17.8	57.4	43.8
τ_1, ns	17.6	20.8	21.25	22.3	20.7
A_2, %	5.6	5.2	5.6	18	6.7
τ_2, ns	87.7	64.5	69.2	72.7	63.6

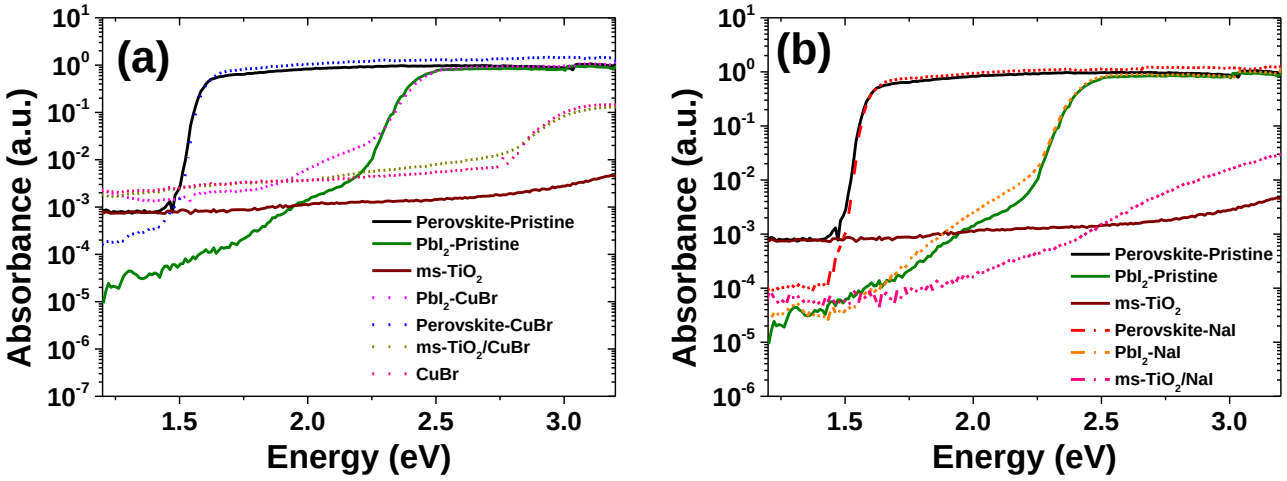

Figure S3. The absorption spectra of pristine and additive based lead iodide and perovskite films as well as additive deposited on ms-TiO_2 and additive only films measured using the PDS technique.

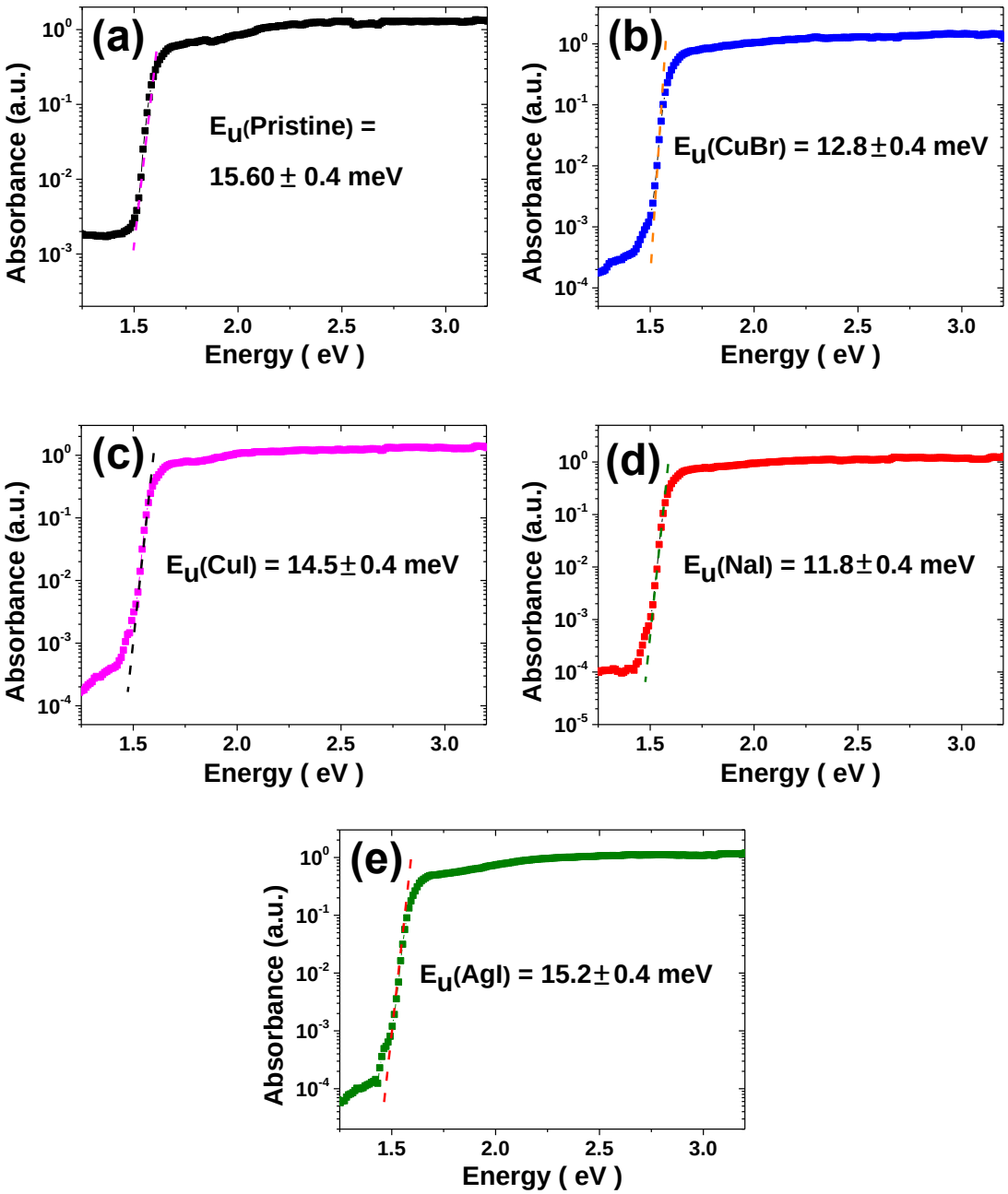

Figure S4. Data fittings of Urbach energy for PDS measurements of perovskite films prepared from (a) pure PbI_2, (b) CuBr, (c) CuI, (d) NaI and (e) AgI based lead iodide. The dotted lines in each plot are the linear fits used to calculate the Urbach energy and the obtained Urbach energy 'Eu' is indicated in each plot. The error indicated in each plot is due to the s.d. in fitting the Urbach tail.

Thickness dependency of charge mobility measurement

As evident from the figure only a small variation of thickness was possible for the devices. It should be noted that varying the thickness of the films in perovskite affects the conversion of the perovskite layer, crystallinity of the material and thus the defect density. Hence, to ensure proper comparison between different thicknesses, devices were carefully chosen such that the current density is minimally affected by external parameters like coverage, crystallite size and grain boundary density for a particular type of materials.

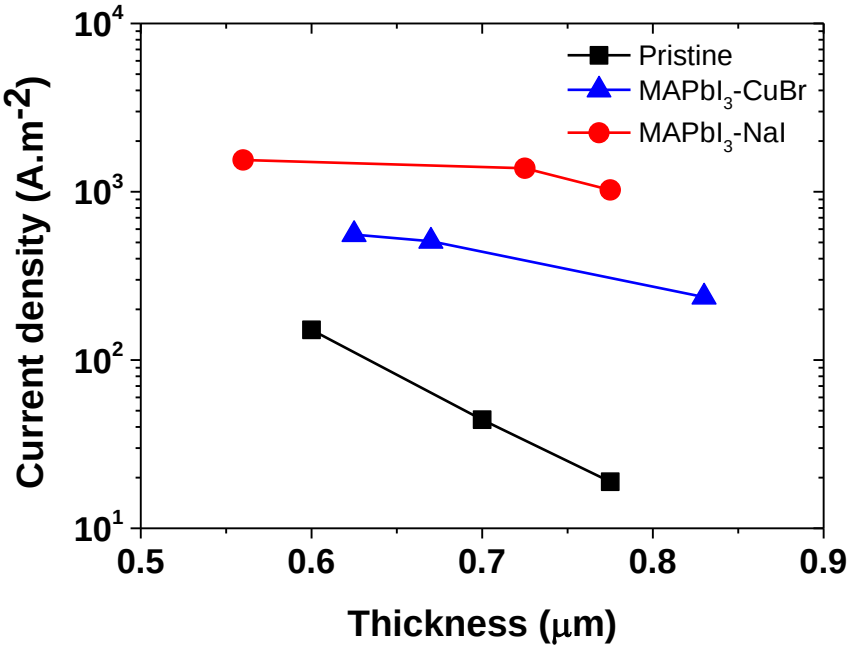

Figure S5. Thickness dependency of measured current density using SCLC method for pristine, CuBr and NaI based perovskite.

Table S2. Summary of the photovoltaic parameters derived from J-V measurements for the pristine and CuBr based perovskite solar cells (batch of 30 devices) with various concentration fabricated using two-step deposition method.

Type of Sample	Dopant Concentration ($mol.l^{-1}$)	J_{SC} ($mA\ cm^{-2}$)	V_{OC} (mV)	FF	PCE (%)
Pristine	-	20.7±0.4	945±13	0.69±0.02	13.7±0.3
CuBr	0.01	22.1±0.6	921±10	0.69±0.03	14.3±0.3
CuBr	0.02	22.5±0.1	948±7	0.70±0.02	15.2±0.4
CuBr	0.04	19.8±0.5	896±16	0.71±0.01	12.6±0.7

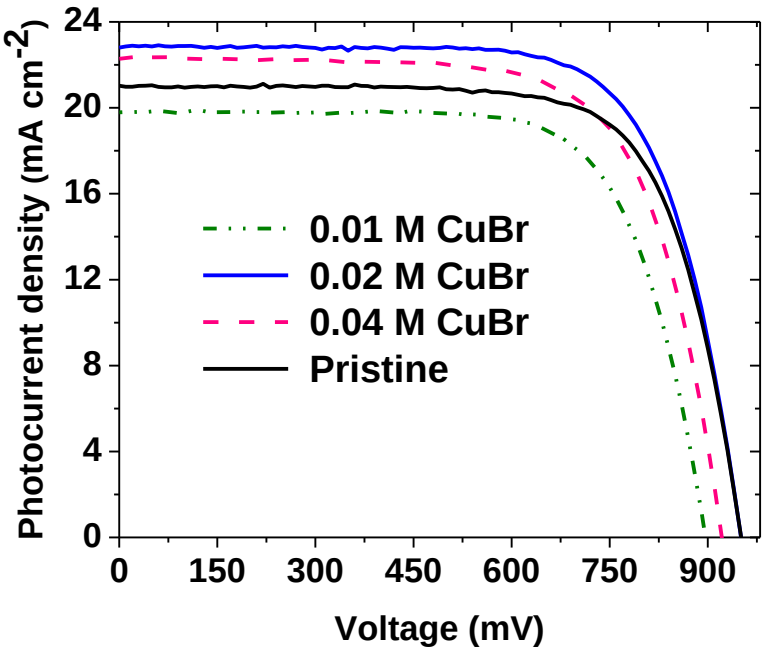

Figure S6. Current-voltage characteristics of devices under illumination of 100 mW cm^{-2} obtained with varying concentration of CuBr additive.

Table S3. Summary of the photovoltaic parameters derived from J-V measurements for the pristine and additive-based perovskite solar cells (batch of 30 devices) fabricated using two-step deposition method.

Type of Sample	J_{SC} (mA cm^{-2})	V_{OC} (mV)	FF	PCE (%)
Pristine	20.7±0.4	945±13	0.69±0.02	13.7±0.3
AgI	19.1±0.1	1007±11	0.71±0.01	14.0±0.2
NaI	22.6±0.2	900±9	0.72±0.02	14.7±0.5
CuI	21.5±0.4	982±14	0.70±0.01	15.0±0.2
CuBr	22.5±0.1	948±7	0.70±0.02	15.2±0.4

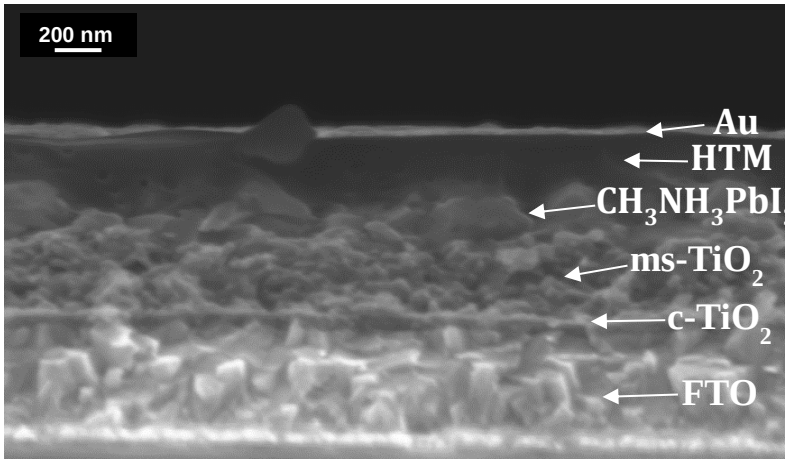

Figure S7. SEM cross sectional micrograph of a complete device having the structure of: FTO/compact TiO_2/mesoporous TiO_2/$CH_3NH_3PbI_3$/Spiro-MeOTAD/Au.

Table S4: Summary of the thickness values for perovskite caping layers on top of mesoporous TiO_2 (measured using a Veeco Dektak 150 profilometer) and FWHM values obtained from the corrsponding lead halide XRD patterns.

Type of Sample	Thickness (nm)	FWHM (2θ) of (001) PbI_2 peak
Pristine	150±20 nm	0.0487
CuBr	170±30 nm	0.0325
CuI	160±20 nm	0.0372
NaI	130±20 nm	0.1467
AgI	190±30 nm	0.0412

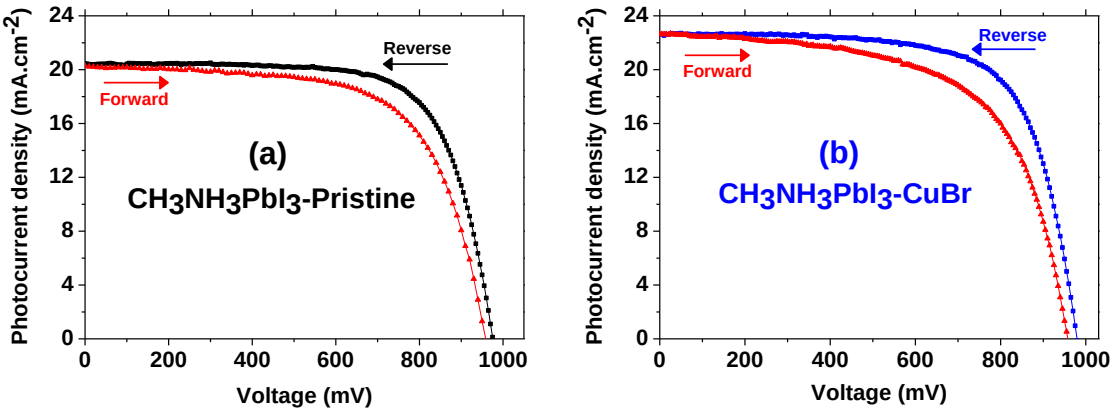

Figure S8. J–V curves for devices fabricated from (a) pristine and (b) CuBr based perovskite measured by forward (short circuit → open circuit) and reverse (open circuit → short circuit) scans with 10 mV voltage steps and 40 ms delay times under AM 1.5 G illumination.

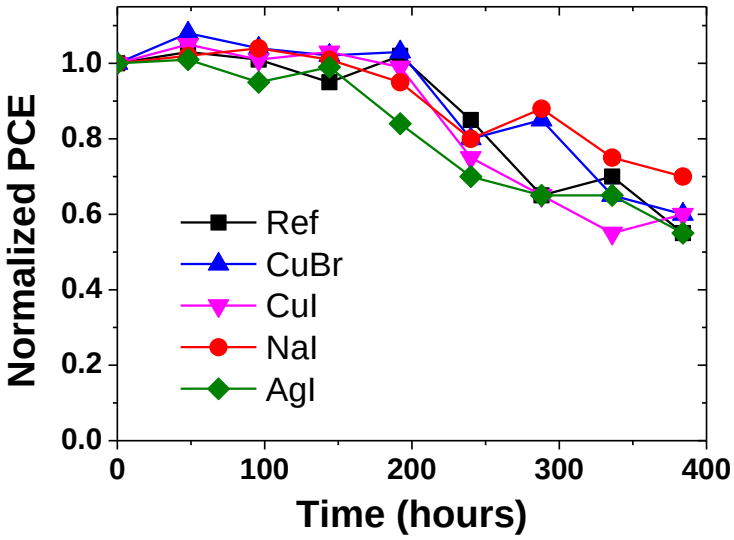

Figure S9. The average value of power conversion efficiency (Normalized PCE) as a function of time for the freshly prepared solar cells is used as the normalization reference value (i.e. for the five types of samples, their initial PCE values are all normalized to 1). The J-V scans were measured under simulated air mass 1.5 global (AM1.5G) solar irradiation. The devices were stored under ambient conditions.

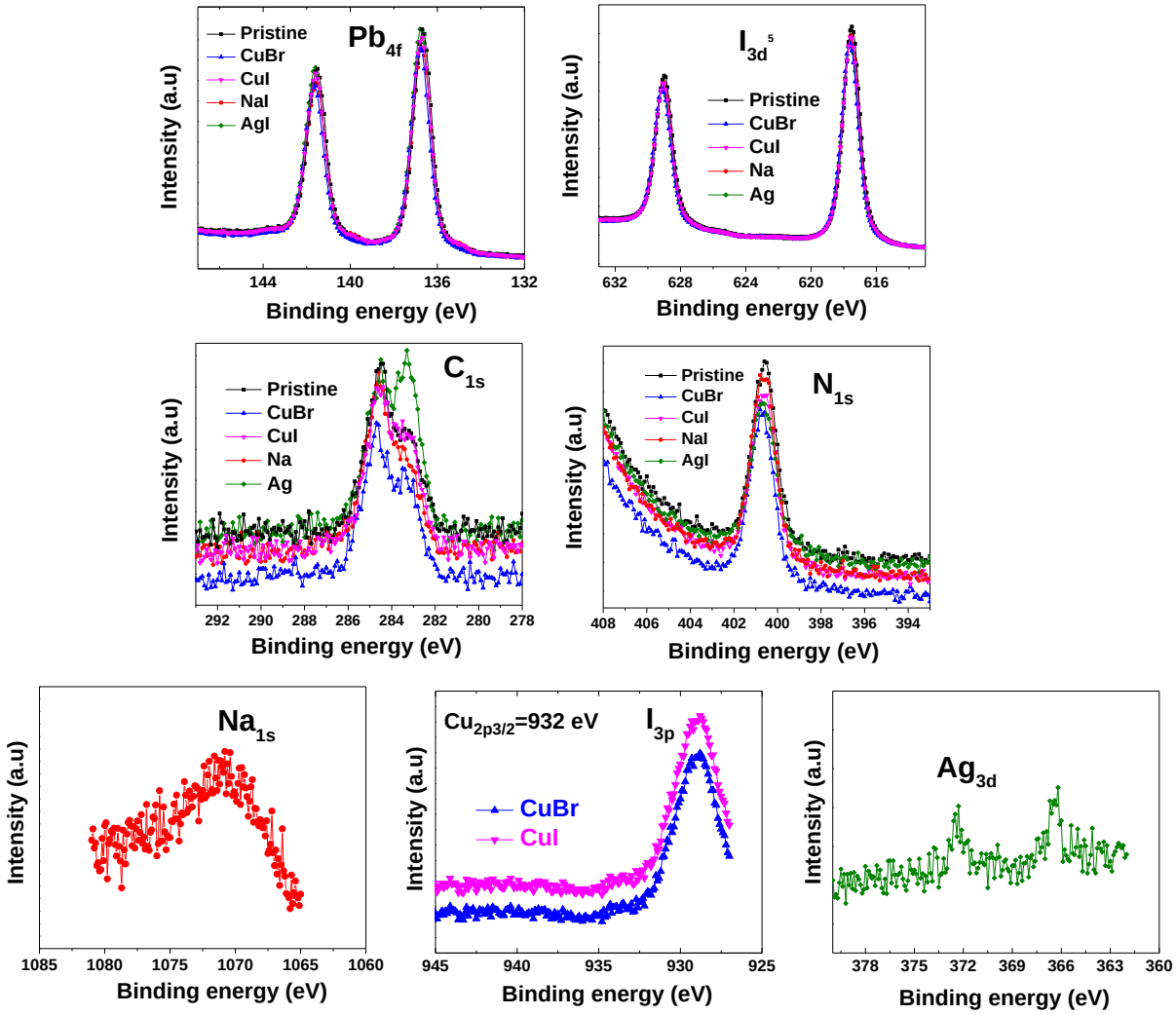

Figure S10. X-ray photoelectron spectroscopic (XPS) analysis of pristine, CuBr-, CuI-, NaI- and AgI-based perovskite films.